

# Microfluidic blood oxygenators with integrated hollow chambers for enhanced air exchange from all four sides

Mohammadhossein Dabaghi<sup>a,1</sup>, Neda Saraei<sup>b,1</sup>, Gerhard Fusch<sup>c</sup>, Niels Rochow<sup>c</sup>, John L. Brash<sup>a,d</sup>, Christoph Fusch<sup>a,c,e</sup>, P. Ravi Selvaganapathy<sup>a,b,\*</sup>

<sup>a</sup> School of Biomedical Engineering, McMaster University, Hamilton, ON, Canada

<sup>b</sup> Department of Mechanical Engineering, McMaster University, Hamilton, ON, Canada

<sup>c</sup> Department of Pediatrics, McMaster University, Hamilton, ON, Canada

<sup>d</sup> Department of Chemical Engineering, McMaster University, Hamilton, ON, Canada

<sup>e</sup> Paracelsus Medical University, Department of Pediatrics, University Hospital Nuremberg, Nuremberg, Germany

## ABSTRACT

Traditionally, cylindrical hollow fibers have been used as gas exchange interfaces in commercial oxygenators due to their simplicity of fabrication and the ability to oxygenate a large volume of blood by flowing blood around a bundle of cylindrical hollow fibers, which are served for the introduction of the gases. Over the past decade, newer microfluidic designs have been developed to overcome some of the limitations of the hollow fiber technology such as the lack of the ability to provide biomimetic flow paths to reduce shear stress and hence potentially initiation of the blood coagulation cascade as well as the difficulty to reduce the distance between fibers to decrease the resistance to diffusion of gases on the blood compartment while achieving higher efficiency of gas exchange. Nevertheless, the microfluidic designs that have been reported in the literature only provide gas exchange interfaces on one or two sides of their rectangular cross-section blood perfusion channels, thereby limiting gas exchange efficiency. Here, we report on a new design where closed gas chambers are placed adjacent to the blood perfusion channels so that the gas exchange into the blood can occur on all four sides. We demonstrate that such a design will increase the gas exchange surface area without affecting the channel's geometry or its flow characteristics. The gas exchange performance of the new design is enhanced up to 223% Compared with its equivalent double-sided gas exchange design. These new designs are expected, in the future, to help microfluidic oxygenators combine the best characteristics of both the microfluidic and hollow fiber designs to achieve superior performance.

## 1. Introduction

Commercial oxygenators that are used clinically are all based on hollow fibers as the fundamental unit through which gas exchange occurs. Hollow fiber-based oxygenators were originally designed such that the blood flows through the hollow fibers, and the exchange gas is perfused through an enclosed jacket surrounding bundles of them [1]. The high flow resistance and the shear stress-induced on the blood in these configurations required a pump for operation as well as increased the chance for hemolysis and thrombotic reaction [1,2] led to current designs which have blood flow in the outer jacket and the exchange gases perfused through the hollow fibers that are coated with silicone or polymethylpentene to eliminate plasma leakage [3–5]. The change in configuration significantly reduces pressure drop but increases the priming volume and lowers gas exchange efficiency, making them unsuitable for small term and pre-term neonates and necessitates

transfusion of blood [6–11]. Furthermore, blood flow in this configuration is not uniform, and stagnation zones, secondary flows, and high shear regions are possible which require high levels of heparinization with consequent deleterious effect on the patient. Recognizing these limitations, microfluidic devices have been developed to provide a more streamlined and uniform flow of blood adjacent to a gas exchange membrane with optimal pressure drop, low priming volume, and reasonable gas exchange capability [12,13]. These devices try to mimic one or several features of the original gas exchange interface: the lung tissue. The huge surface-area-to-blood-volume ratio ( $300 \text{ cm}^{-1}$ ) and its small thickness ( $1 - 2 \mu\text{m}$ ) which provide high permeability to gases as well as the small size of the blood perfusion channels which provide excellent gas transfer efficiency [14,15] have been the driving factors in many microfluidic designs [6,8–10,13,16–25] although these features have not been entirely achieved [12]. Although considerable progress has been made in microfluidic designs of the blood oxygenators, they

\* Corresponding author. Department of Mechanical Engineering, McMaster University, 1280, Main Street West, Room JHE 212B, Hamilton, Ontario, L8S 4L7, Canada.

E-mail address: [selvaga@mcmaster.ca](mailto:selvaga@mcmaster.ca) (P.R. Selvaganapathy).

<sup>1</sup> These authors contributed equally to this work.

<https://doi.org/10.1016/j.memsci.2019.117741>

Received 19 August 2019; Received in revised form 8 December 2019; Accepted 9 December 2019

Available online 12 December 2019

0376-7388/© 2019 Elsevier B.V. All rights reserved.

still exchange oxygen with the supply gas either on one or two sides [9, 11,18,25] of their microfluidic network. Therefore, two or three other sides of the blood microchannels will not be involved in gas exchange.

Gas transfer in microfluidic devices can be enhanced further if all four sides of the blood perfusion channels were to be exposed to oxygen through the gas exchange membrane. However, fabricating such a device configuration is technologically challenging. Instead in this paper, we introduce a new concept where a closed gas holding chamber is fabricated on either side of the blood channel. The large capacity of the holding chamber then allows adequate perfusion of gases from sides, which in combination with the exchange from the top and the bottom side can improve the gas transfer efficiency. We describe the design and fabrication of such oxygenators, termed four-sided microfluidic blood oxygenator (fsMBO), and identify the optimal size of the air chambers. We also demonstrate that the performance of such devices are superior to equivalent two-sided devices.

## 2. Design

### 2.1. Microfluidic device design

The new four-sided microfluidic blood oxygenator consisted of a blood flow path, named as a blood “vascular network,” two composite membranes on each side of the blood vascular network, and an array of sealed hollow air chambers adjacent to blood channels. The blood vascular network was designed as a branched network to smoothly distribute the blood coming from a single inlet into 32 straight microchannels that were 20 mm long and 110  $\mu\text{m}$  wide. To maintain the pressure drop low enough for a pumpless operation, no height lower than 70  $\mu\text{m}$  was studied. Moreover, the length of the blood microchannel was chosen to be 20 mm to avoid high pressure drops and be able to fit 32 microchannels with their distribution channels in a 3-inches wafer (the optimization analysis for choosing the dimension of the blood channels is discussed in detail in the *Supplementary*, section 1.1). A 3D schematic view of the device is depicted in Fig. 1a showing the branching network, which was designed based on Murray’s law (for dimension of channels and not branching angles) [26,27]. The blood vascular network was fabricated with three different heights of 70, 85, and 110  $\mu\text{m}$  for comparison purposes. Both composite membranes were made of polydimethylsiloxane (PDMS) and an ultra-thin stainless-steel mesh (MS-400/19, Asada Mesh Co., Ltd.). PDMS (Sylgard 184, Dow Corning, Midland, MI) was chosen due to its high gas permeability [28], and the ultra-thin stainless-steel mesh was used to reinforce PDMS resulting in a significant enhancement in the composite membrane’s mechanical properties [9,10]. The bottom membrane was  $\sim 48 \mu\text{m}$  thick, and the top membrane had a thickness of  $\sim 90 - 106 \mu\text{m}$ . In this design, the hollow air chambers adjacent to the blood channels acted as

air pockets to provide gas exchange from the side membranes of the blood channels. These chambers were optimized to be 1 mm wide and were separated from the blood flow channels by a wall that was  $\sim 88 \mu\text{m}$  in thickness, named as side membranes. The 88  $\mu\text{m}$ -thick side membrane through which gas exchange can occur was the thinnest that could be reliably produced with the current fabrication technology. For comparison purposes, a device without air chambers, termed as double-sided microfluidic blood oxygenator (dsMBO), was also manufactured. Table 1 summarizes the design parameters for all fsMBOs. Fig. 1b shows an SEM image of a fully fabricated fsMBO’s mold with the regions for hollow air chambers and the blood channels shaded in blue and red.

### 2.2. Design of hollow air chambers

In fsMBO design, hollow air chambers play an essential role, and there was a need to understand how the dimension of these hollow chambers would impact the total oxygen transfer. As a result, a numerical simulation of the transport of oxygen through the device under various operating conditions was performed using COMSOL Multiphysics software in order to determine the size of the hollow air chambers. A simple 2D model consisting of an air chamber flanked on either side by two blood channels and with thin gas permeable membranes on the top and the bottom (Fig. 2a) was used. The initial and boundary conditions for the simulation are provided in the *supplementary section 1.2*. In order to simplify the simulation, no convection was assumed within the air chamber, and a constant concentration of oxygen (68% saturation and 50 mm Hg) was considered for the blood to mimic steady-state conditions of the incoming blood to the oxygenator. It is expected that the oxygen flux from the chamber into the blood channel through the side membranes will be the highest in the regions near the inlet where the incoming deoxygenated blood interacts with thin membranes from all sides and starts getting oxygenated, and therefore that condition was chosen for simulation and to size the air chambers. In this model, the height of the air chamber was constant at 110  $\mu\text{m}$  while the width of the chamber was varied from 100 – 2000  $\mu\text{m}$  (this range was chosen because the width of the blood channel in fsMBOs was around 110  $\mu\text{m}$  and chamber sizes wider than 2000  $\mu\text{m}$  would occupy disproportionately larger volume that may make the design not feasible for implementation). The thickness of the top, bottom, and side membranes were defined based on the corresponding dimension of the real device. All numerical analysis performed in COMSOL Multiphysics for this section were time-dependent. All the parameters reported were from the center of the hollow air chamber.

As a first step, the change in the oxygen partial pressure in the hollow air chamber was simulated over time (200 s) for various widths (Fig. 2b). The oxygen partial pressure was found to initially decrease with time and quickly reached an equilibrium. However, the partial equilibrium

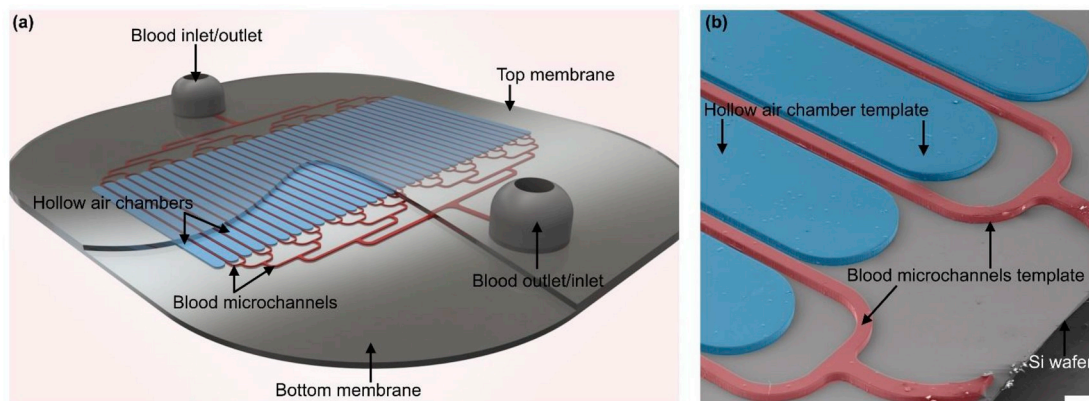


**Fig. 1.** (a) a 3D schematic view of a fsMBO and (b) SEM image (in false color) of the fsMBO’s mold showing the branching network and air chambers. The scale bar is 200  $\mu\text{m}$ . (For interpretation of the references to color in this figure legend, the reader is referred to the Web version of this article.)

**Table 1**

Design parameters for fsMBOs. SAV stands for surface area to volume ratio. Data are means  $\pm$  SD. N = 5. Effective surface area, priming volume, and SAV only account for gas transfer channels not the branching channels.

Height ( $\mu\text{m}$ )	Effective surface area ( $\text{mm}^2$ )	Priming volume ( $\text{mm}^3$ )	SAV ( $\text{cm}^{-1}$ )	Top membrane thickness ( $\mu\text{m}$ )	Bottom membrane thickness ( $\mu\text{m}$ )	Side membranes ( $\mu\text{m}$ )
$69.4 \pm 3.4$	229.6	4.88	469	$90.8 \pm 16.4$	$48.4 \pm 3.2$	$87.8 \pm 3.2$
$85.8 \pm 3.4$	250.6	6.04	415	$100.2 \pm 4.5$	$48 \pm 2.0$	$88 \pm 2.7$
$110.6 \pm 2.4$	282.4	7.79	362	$106.8 \pm 4.9$	$48 \pm 2.4$	$88 \pm 3.7$

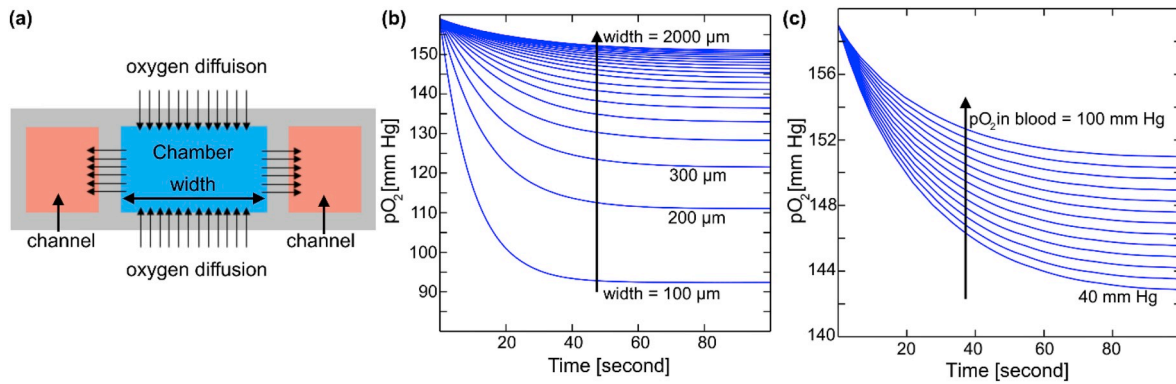


**Fig. 2.** (a) 2D schematic cross-sectional view of an air chamber adjacent to two blood microchannels used in computer modeling showing the direction of oxygen diffusion, (b) the numerical result of the final oxygen partial pressure in the air chamber over time for different width while the blood microchannels are filled with blood having a constant dissolved oxygen content of 50 mm Hg, and (c) the numerical result of the oxygen partial pressure in the air chamber with a width of 1  $\mu\text{m}$  and a height of 110  $\mu\text{m}$  versus different dissolved oxygen concentrations in the blood microchannels.

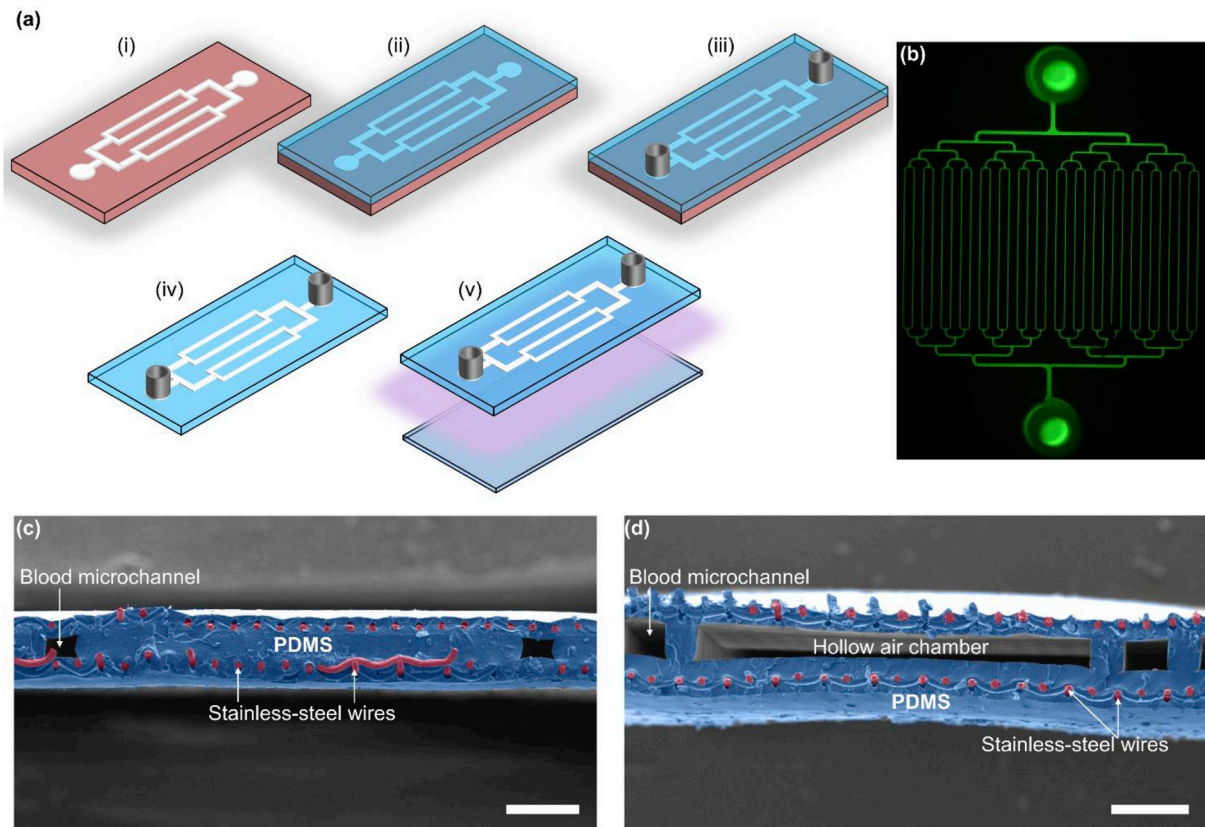


**Fig. 3.** (a) the fabrication process of both dsMBOs and fsMBOs, (b) a wide-field-of-view fluorescent image of the blood vascular network filled with DI water and a fluorescent dye, (c) a SEM image of the cross-sectional view of a dsMBO (without air chambers), and (d) a SEM image of the cross-sectional view of a fsMBO. All scale bars are 200  $\mu\text{m}$ .



pressure was strongly dependent on the size of the air chamber. The concentration of the oxygen in the air chamber is determined by two fluxes. The ratio of fluxes into the air chamber from the outside environment through the top and the bottom membrane to that out of the air chamber through the side membranes determine the equilibrium. Equilibrium partial pressure changed significantly when the chamber dimensions were increased from 100–200  $\mu\text{m}$ , but the change decreases as the chamber size is increased further. Beyond 1000  $\mu\text{m}$  the difference is minimal, and there was no benefit to increase in chamber size. Once this dimension was chosen, simulations were performed to determine the influence of the oxygen concentration in the blood microchannels on the equilibrium oxygen concentration for the air chamber (Fig. 2c). The partial pressure of oxygen in the blood channels changed from 40 mm Hg to 100 mm Hg (a typical range), and the equilibrium oxygen concentration was depicted over time. The changes in oxygen concentration on the blood side had a minimal impact (with only a small difference of  $\sim 8$  mm Hg) on equilibrium oxygen partial pressure inside the chamber when its dimension was 1000  $\mu\text{m}$  in width, indicating that this width is optimal to maintain a suitable oxygen partial pressure close to the side membranes and facilitate four-sided oxygenation.

### 3. Experimental

#### 3.1. Fabrication of microfluidic devices

The negative template of both blood vascular networks (fsMBOs and dsMBO) was made by photolithography using a SU-8 photoresist (SU-8 100, Microchem Corp, Westborough, MA, USA) as depicted in Fig. 3a.i. The surface of all molds was coated with a thin layer of trichloro (1H,1H,2H,2H-perfluorooctyl) silane (Sigma Aldrich) by chemical vapor deposition to facilitate ease of delamination from the molds.

The fabrication (Fig. 3a) of both dsMBOs and fsMBOs was performed using a spin-coater to precisely control the thickness of each layer. PDMS base and curing agent were mixed in 10:1 ratio and degassed in a desiccator for removing all air bubbles. PDMS was poured on the molds and spin-coated with a specific RPM for each height (1100 RPM for the mold with a height of 70  $\mu\text{m}$ , 950 RPM for the height of 85  $\mu\text{m}$ , and 850 RPM for the height of 110  $\mu\text{m}$ ) so that the PDMS fills that gap between the mold features and then forms a thin membrane layer of the same thickness for all of the mold heights. The mold with spin-coated PDMS was vacuumed by a desiccator to ensure that no air bubble was trapped between blood channels and hollow air chambers. This step was repeated as many times as needed until no air bubble was observed. PDMS was cured on a leveled hot plate at 85  $^{\circ}\text{C}$  for 30 min. The second layer of PDMS was spin-coated on top of the mold at a speed of 4000 RPM for 40 s. Then a piece of the ultra-thin stainless-steel mesh, cut with two holes for inlet and outlet [9], was placed onto wet PDMS film and partially cured on a hot plate at 85  $^{\circ}\text{C}$  for 30 min. Another PDMS layer was spin-coated onto this composite at 4000 RPM for 40 s to embed the stainless-steel mesh and surround it entirely with PDMS (Fig. 3a.ii). Two silicone tubes were attached at the designated locations for inlet and outlet using wet PDMS and cured in an oven at 85  $^{\circ}\text{C}$  for 30 min (Fig. 3a.iii). The blood vascular network thus formed was ready to be peeled off from the mold, and any residual PDMS left inside tubes were carefully removed by a biopsy puncher and a scalpel (Fig. 3a.iv). The second composite membrane (the bottom one) was prepared by spin-coating a thin layer of PDMS (4000 RPM for 40 s) on a substrate followed by embedding a piece of the ultra-thin stainless-steel mesh onto wet PDMS. This composite was cured at 85  $^{\circ}\text{C}$  for 30 min and was coated with another PDMS layer (4000 RPM for 30 s) [9,10]. Next, the blood vascular network and the composite membrane were bonded by means of an oxygen plasma at 45 W power for 1.5 min and an oxygen pressure of 900 mm Torr (Fig. 3a.v). The bond strength was improved by a post-baking at 85  $^{\circ}\text{C}$  overnight.

The completed device was filled with a fluorescent dye for visualization, as shown in Fig. 3b. Fig. 3c and d show the SEM images of the

cross-sectional view of a dsMBO and a fsMBO, respectively, showing the placement of air cavities adjacent to the blood channels. The device was pressure tested up to 300 mmHg to ensure that the bonding was strong and the device was leakproof.

#### 3.2. Experimental set-up for gas exchange testing

The bovine blood was purchased from Cedarlane (Burlington, ON, Canada) and heparinized with a concentration of 6 units per ml. Once the blood was delivered, its oxygen saturation level ( $\text{SaO}_2$ ) was adjusted to venous conditions ( $68 \pm 1.2\%$ ) using the method developed previously [9,18] and stored in a fridge overnight. Briefly, the blood was fed to the shell of a commercial hollow fiber (PDMSXA-1.0, PermSelectVR, Ann Arbor, MI, USA), where a mixture of  $\text{N}_2$  and  $\text{CO}_2$  (5%/95%, v/v) was sent to the fibers. To ensure the desired level ( $\sim 68\%$ ) was achieved, the  $\text{SaO}_2$  was usually set to a lower value around 60% before storing in the fridge. Then, the blood in the container was sealed and stored overnight in the fridge at 4  $^{\circ}\text{C}$ . A gas exchange would occur between the gases above the blood, and the blood and the blood would reach an equilibrium overnight. Storing the blood at 4  $^{\circ}\text{C}$  would also minimize the oxygen metabolism by cells. Before testing each device, the blood was transferred to a 140 mL-syringe with a stir bar, which provided a continuous mixing in the blood to maintain the blood homogeneous throughout testing. A fast and secure transfer of the blood into syringes would guarantee a low shift in  $\text{SaO}_2$  (usually 1–3%). The blood was perfused through devices with various blood flow rates of 0.16  $\text{mL min}^{-1}$ , 0.32  $\text{mL min}^{-1}$ , 0.64  $\text{mL min}^{-1}$ , 0.96  $\text{mL min}^{-1}$ , and 1.28  $\text{mL min}^{-1}$  while devices were exposed to room air. Four dsMBOs and three fsMBOs for each height were tested with blood in room air. Also, one fsMBO was tested in an oxygen-rich environment.

A point-of-care blood gas analyzer (GEM Premier 3000, Instrumentation Laboratory, Lexington, MA, USA) was used to evaluate the gas content in blood before and after each device. Blood samples were taken before and after fsMBOs to monitor any potential hemolysis (Fig. S5 in the supplementary) by centrifuging blood using a Complete Micro-Hematocrit System (StatSpin CritSpin, Norwood, MA, USA). Two 3-ways connectors were placed before and after each device. The purpose of these 3-ways connectors was to assure that no air was introduced to blood samples. To achieve this matter, first 1 mL blood was collected from each 3-ways connector and discarded. Then,  $\sim 0.4$  mL of blood syringe was collected in a new 1-mL and capped to prevent the exposure to room air. In this way, the blood samples would not be compromised by exposure to room air.

Blood gas properties measured by the blood gas analyzer were used to calculate the oxygen transfer and the carbon dioxide transfer using the methods and equations described somewhere else [6,29]. Briefly, the oxygen content of the blood was calculated by summing the amount of dissolved oxygen and the amount of oxygen bonded to hemoglobin. Carbon dioxide content was calculated by assuming carbon dioxide in both phases of plasma and erythrocyte fluid.

### 4. Results and discussion

#### 4.1. Comparison between the performance of dsMBOs and fsMBOs

To demonstrate the improvement in the performance of fsMBO design over the more conventional dsMBO, oxygenators with similar geometries were fabricated. The dsMBO design used for this purpose had the air chambers filled with PDMS but was otherwise identical to the fsMBO design. It also had a slightly thinner top membrane ( $\sim 90$   $\mu\text{m}$  compared with  $\sim 100$   $\mu\text{m}$ ) which is expected to have a negligible effect on oxygen diffusion into the device as the rate limitation is mainly limited due to diffusion in the blood plasma and not the membrane thickness at these scales [9,12]. Both had a bottom membrane with the same thickness of  $\sim 50$   $\mu\text{m}$ . Blood flow rates of 0.16, 0.32, 0.64, 0.96, 1.28  $\text{mL min}^{-1}$  were used while the devices were tested in room air. Four

dsMBOs and three fsMBOs with the same height of  $\sim 70 \mu\text{m}$  for blood microchannels were evaluated.

The measurement of various performance characteristics, including the increase in oxygen saturation of blood as well as the oxygen and carbon dioxide transfer across the membrane for both the dsMBOs and fsMBOs, are shown in Fig. 4. The increase in oxygen saturation ( $\Delta\text{SaO}_2$ ) between the inlet and the outlet for dsMBOs gradually decreased with increase in flow rate due to a consequent decrease in residence time for red blood cells (RBC) inside the oxygenator (Fig. 4a). Although  $\Delta\text{SaO}_2$  for fsMBOs (Fig. 4a) followed a similar trend, it was consistently higher than dsMBOs and seemed to plateau at higher blood flow rates ( $1.28 \text{ mL min}^{-1}$  as opposed to  $0.96 \text{ mL min}^{-1}$  for dsMBOs). This increase in performance is likely due to the lateral oxygen transport from the hollow air chambers to the sides of the blood channels in addition to the transport from the top and bottom membranes. A similar trend and behavior were also measured for the increase in the partial pressure of oxygen ( $\Delta\text{pO}_2$ ) in the blood (Fig. 4b). These observations are expected based on the relationship between  $\text{SaO}_2$  and  $\text{pO}_2$  are provided by the Hill's equation [30,31].

However, the calculation of the net oxygen transfer to the blood showed a difference in trend with an increase in flow rate when dsMBOs and fsMBOs were compared (Fig. 4c). In the case of dsMBOs, the average oxygen transfer remains nearly the same irrespective of the flow rates tested. This is in contrast with the fsMBOs, which show an increase in the overall oxygen transfer with flowrate. Even at low flow rates there is a significant difference between the two designs in the amount of oxygen transferred and this difference increases with flow rate. The average carbon dioxide transfers also followed similar trends for both dsMBOs and fsMBOs (Fig. 4d). To quantify the improvement in the performance, the average oxygen transfer of fsMBOs was compared to dsMBOs by calculating the percentage increase of the average oxygen transfer of fsMBOs from that of dsMBOs (Fig. 4e). As expected, the improvement in performance increased with increasing blood flow rate in a manner similar to the improvement in the performance of dsMBOs compared to single-sided microfluidic blood oxygenators as reported previously [9].

Finally, the increase in oxygen saturation was numerically modeled using COMSOL Multiphysics software for the fsMBO design at the tested blood flow rates (the computational fluid dynamics models are explained in detail in the supplementary, section 1.3). As can be seen in Fig. 4f, the experimental data for increase in oxygen saturation in this design closely matched the simulation results and followed a similar trend. Simulation results for the change in oxygen saturation of the blood as it flows in the oxygenator is presented in the supplementary (Fig. S4) for the maximum and minimum flow rates that were experimentally tested. It shows the uniformity of the increase in saturation as the blood transits the oxygenator. Finally, the oxygenator was also tested over a more extended period (90 min) with steady perfusion of blood to determine if the oxygenation performance was stable. The results shown in the Supplementary section 3 show that blood gas parameters were stable over that duration of time, indicating that concentration of oxygen in the closed air chambers quickly settled into a stable value and sustained the oxygenation of the blood through the side membranes.

#### 4.2. In vitro assessment of hollow air chambers in open and closed configurations

The sealed air chambers were incorporated into the design of the oxygenator, primarily due to the ease of their integration. However, the concentration of oxygen in these chambers will be lower than the ambient, which will have an impact in reducing the efficiency of oxygen transfer. An alternate approach can be to have air chambers that are open to the outside ambient and capable of quickly equilibrating with it. In order to determine the impact of open vs. closed chambers, several fsMBO's were tested first with sealed air chambers followed by testing with the hollow air chambers carefully cut open by a scalpel to expose them to the ambient. The oxygenators were tested in an ambient of 100% oxygen at atmospheric pressure in order to determine the maximum difference in oxygenation performance between the two configurations as well as to identify the performance of fsMBOs in a pure oxygen

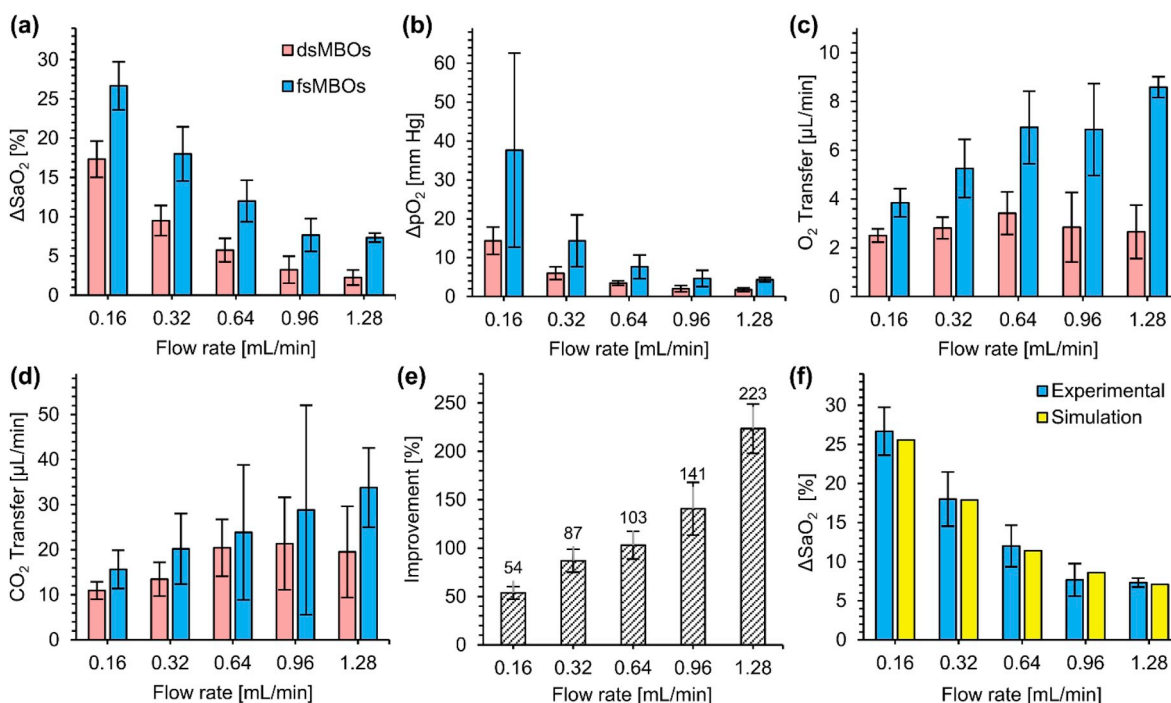


**Fig. 4.** In vitro comparison between dsMBOs and fsMBOs using air as the sweep gas: (a) the increase in oxygen saturation level ( $\Delta\text{SaO}_2$ ), (b) the increase in partial pressure of oxygen ( $\Delta\text{pO}_2$ ), (c) the oxygen transfer, (d) the carbon dioxide ( $\text{CO}_2$ ) transfer, (e) the improvement in the oxygen transfer of fsMBOs compared to dsMBOs, and (f) the comparison between the experimental data and numerical simulation for fsMBOs. Data are means  $\pm$  SD. All devices were tested in room air. Four dsMBOs and three fsMBOs tested.

environment. In this experiment, the device was placed in a sealed chamber, which was later filled with 100% oxygen. The devices were also tested at higher blood flow rates (0.64, 1.28, 1.92, 2.56 mL min<sup>-1</sup>) since the device could fully oxygenate the blood at a blood flow rate of 0.64 mL min<sup>-1</sup> (increase of SaO<sub>2</sub> from 65% to 100%).

The change in the measured oxygen saturation level from these experiments is presented in Fig. 5a. In both configurations,  $\Delta\text{SaO}_2$  continuously decreased with flow rate due to the lower residence time of the blood in the device.  $\Delta\text{pO}_2$  also displayed a similar trend to the oxygen saturated level (Fig. 5b). The oxygen transfer slightly increased for the device with closed chambers and reached a stable value at a blood flow rate of 1.28 mL min<sup>-1</sup> (Fig. 5c). The trend for oxygen flux for the device with open chambers was different with a gradual increase over tested blood flow rates (Fig. 5c). The difference in oxygen flux between the open and closed configurations increased with flow rate (Fig. 5c). At low flow rates, both configurations oxygenate the incoming blood to 100% saturation, which forms a ceiling. However, at higher flow rates, the oxygen partial pressure in the closed chamber will be lower than that in the open chamber. This results in a more considerable flux of oxygen through the side membranes and into the blood results in a high oxygen transfer as compared with the closed chamber. For carbon dioxide transfer, a more significant difference between the close and open chambers was observed (Fig. 5d). This could be attributed to the higher permeability of carbon dioxide compared to oxygen through PDMS. Although proof of concept has been demonstrated of the open air chamber configuration, a more reliable fabrication approach needs to be developed, and the robustness of the device, especially against bond failure and leakages have to be evaluated.

#### 4.3. The effect of the channel's height

Finally, fsMBOs with three different heights were fabricated and

tested with bovine blood to assess the impact of the channel's height on their gas exchange capacities. In general, it was found that changing height from 70  $\mu\text{m}$  to 110  $\mu\text{m}$  would not noticeably compromise the gas exchange performance (Fig. 6). Fig. 6a shows the increase in oxygen saturation level with respect to flow rate. For all three heights,  $\Delta\text{SaO}_2$  decreases with an increase in blood flow rates due to lower residence time for blood microchannels; therefore, the gas transfer became limited to the regions adjacent to four membranes. The same trend was observed for the increase in oxygen partial pressure (Fig. 6b). Oxygen transfer (Fig. 6c) and carbon dioxide transfer (Fig. 6d) were gradually increased when blood flow rates were increased. This suggested that increasing the height to 110  $\mu\text{m}$  would not significantly affect the gas exchange capacity of the device but can lower pressure drop in the device.

## 5. Conclusion

A new design for microfluidic blood oxygenators where a gas transfer can occur from all four sides of the blood capillary network was introduced. This was achieved by integrating a closed air chamber between the adjacent blood microchannels which could serve as reservoir of air that could enable oxygen flux through the side membranes of the blood channels. We demonstrate that there is a significant difference in oxygenation performance between the fsMBOs and dsMBOs. We also show that an open air chamber, as opposed to a closed one, can further improve oxygenation performance and this improvement is greater at higher flow rates. Although proof of the concept of the four-sided configuration has been demonstrated, this device needs to be scaled up to meet practical clinical requirements of neonates. The modular nature of the design and the simple fabrication process can enable scaling up of this design to handle larger blood flow rates in the future.

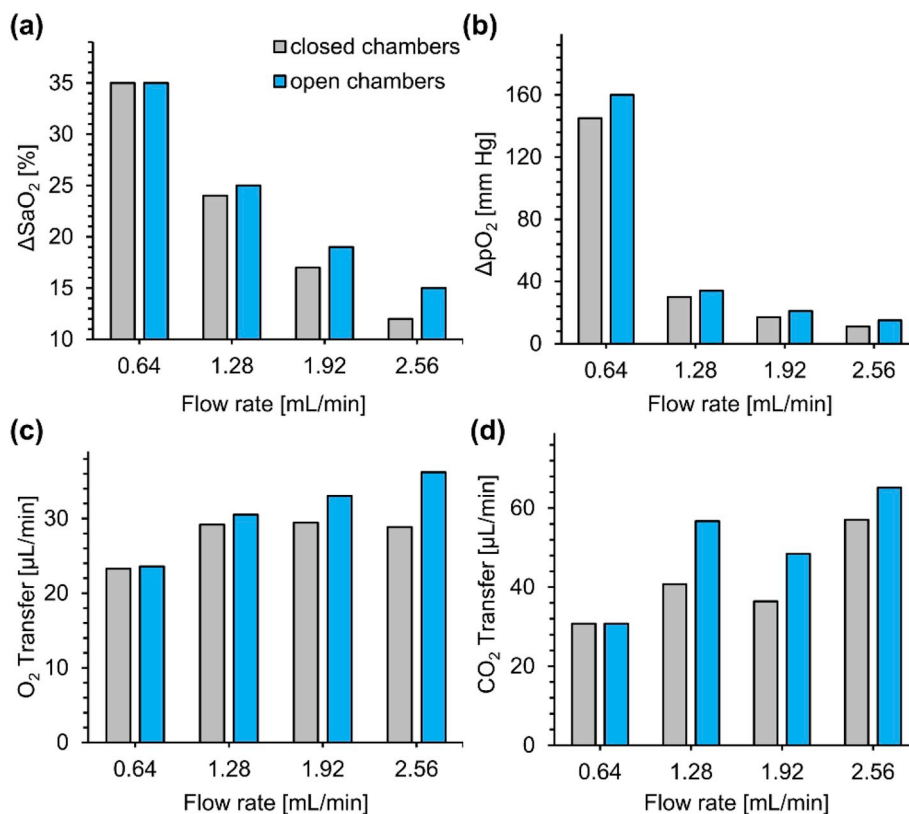


**Fig. 5.** In vitro  $\Delta\text{SaO}_2$  comparison between a fsMBO with open and closed air chambers tested in a pure oxygen environment with atmospheric pressure (a) the increase in oxygen saturation, (b) the increase in the oxygen partial pressure, (c) oxygen transfer, and (d) carbon dioxide transfer. The comparison was made between a fsMBO with open and closed air chambers tested in pure oxygen.  $n = 1$ .

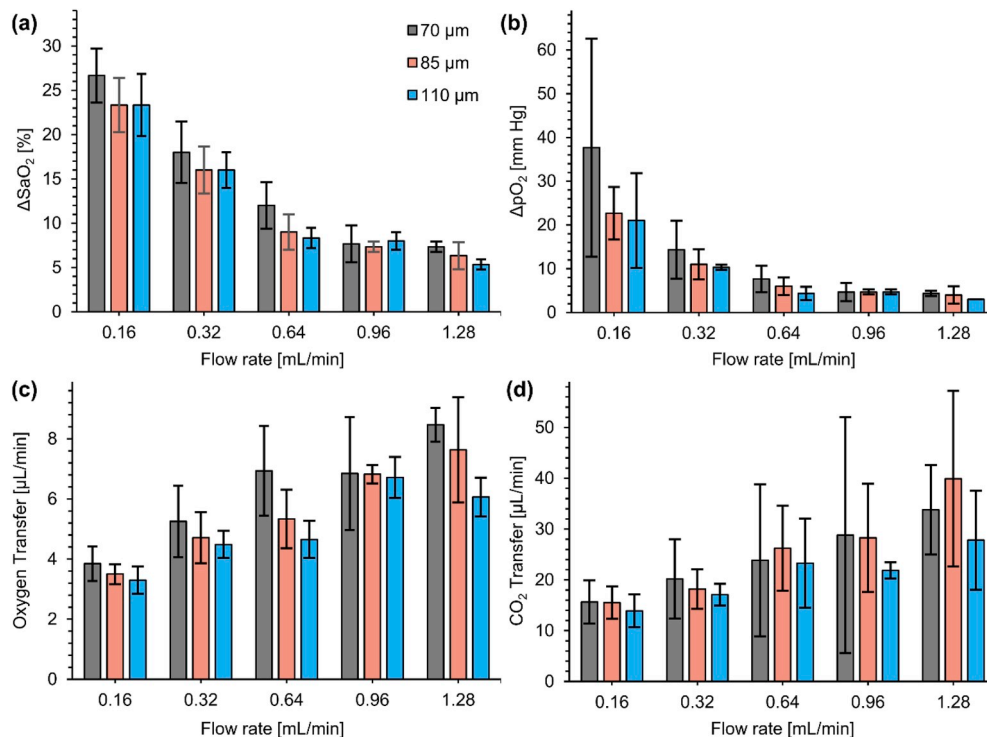


**Fig. 6.** In vitro gas exchange testing with bovine blood for fSMBOs with three different heights of 70  $\mu\text{m}$ , 85  $\mu\text{m}$ , and 110  $\mu\text{m}$  with respect to flow rate while they were exposed directly to room air: (a) the increase in oxygen saturation level, (b) the increases in oxygen partial pressure, (c) oxygen transfer and (d) carbon dioxide transfer. Data are mean  $\pm$  SD,  $n = 3$ .

### Declaration of competing interest

The authors have no conflict or interests to declare. All the funding for this work was obtained through national funding agencies.

### Acknowledgments

This work was supported by the Natural Sciences and Engineering Research Council of Canada (NSERC) and Canadian Institutes of Health Research (CIHR) through the Collaborative Health Research Program. PRS also acknowledges support from the Canada Research Chairs Program as well as the Discovery Accelerator Supplement grant. CF acknowledges support from Jack Sinclair Research Chair position at McMaster University.

### Appendix A. Supplementary data

Supplementary data to this article can be found online at <https://doi.org/10.1016/j.memsci.2019.117741>.

### References

- [1] T. Yeager, S. Roy, Evolution of gas permeable membranes for extracorporeal membrane oxygenation, *Artif. Organs* 41 (2017) 700–709, <https://doi.org/10.1111/aor.12835>.
- [2] W.J. Federspiel, K.A. Hench, in: G.L. Bowlin, G. Wnek (Eds.), *Lung, Artificial: Basic Principles and Current Applications*, *Encycl. Biomater. Biomed. Eng. Ed.*, Marcel Dekker, New York, 2004, pp. 910–921, <https://doi.org/10.1081/E-EBBE> (2004).
- [3] H.J. Eash, H.M. Jones, B.G. Hattler, W.J. Federspiel, Evaluation of Plasma Resistant Hollow Fiber Membranes for Artificial Lungs, *FE*, 2004, <https://doi.org/10.1097/01.MAT.0000138078.04558>.
- [4] J.M. Toomasian, R.J. Schreiner, D.E. Meyer, M.E. Schmidt, S.E. Hagan, G. W. Griffith, R.H. Bartlett, K.E. Cook, A polymethylpentene fiber gas exchanger for long-term extracorporeal life support, *Am. Soc. Artif. Intern. Organs J.* 51 (2005) 390–397, <https://doi.org/10.1097/01.mat.0000169111.66328.a8>.
- [5] C. Marcelo, S. Keshavjee, Artificial lung support, in: *Regen. Med. Appl. Organ Transplantation*, Elsevier Inc. Netherlands, 2014, pp. 683–689, <https://doi.org/10.1016/B978-0-12-398523-1.00071-9>.
- [6] W.-I. Wu, N. Rochow, E. Chan, G. Fusch, A. Manan, D. Nagpal, P. R. Selvanapathy, C. Fusch, Lung assist device: development of microfluidic oxygenators for preterm infants with respiratory failure, *Lab Chip* 13 (2013) 2641, <https://doi.org/10.1039/c3lc41417e>.
- [7] N. Rochow, E.C. Chan, W.-I. Wu, P.R. Selvanapathy, G. Fusch, L. Berry, J. Brash, A.K. Chan, C. Fusch, Artificial placenta - Lung assist devices for term and preterm newborns with respiratory failure, *Int. J. Artif. Organs* 36 (2013) 377–391, <https://doi.org/10.5301/ijao.5000195>.
- [8] N. Rochow, A. Manan, W.-I. Wu, G. Fusch, S. Monkman, J. Leung, E. Chan, D. Nagpal, D. Predescu, J. Brash, P.R. Selvanapathy, C. Fusch, An integrated array of microfluidic oxygenators as a neonatal lung assist device: in vitro characterization and in vivo demonstration, *Artif. Organs* 38 (2014) 856–866, <https://doi.org/10.1111/aor.12269>.
- [9] M. Dabaghi, G. Fusch, N. Saraei, N. Rochow, J. I. Brash, C. Fusch, P. R. Selvanapathy, An artificial placenta type microfluidic blood oxygenator with double-sided gas transfer microchannels and its integration as a neonatal lung assist device, *Biomechanics* 12 (2018), <https://doi.org/10.1063/1.5034791>, 044101.
- [10] H. Matharoo, M. Dabaghi, N. Rochow, G. Fusch, J. Brash, C. Fusch, P. R. Selvanapathy, Steel reinforced composite silicone membranes and its integration to microfluidic oxygenators for high performance gas exchange, *Biomechanics* 12 (2018), 014107.
- [11] M. Dabaghi, N. Saraei, G. Fusch, N. Rochow, J.L. Brash, C. Fusch, P. Ravi Selvanapathy, An ultra-thin, all PDMS-based microfluidic lung assist device with high oxygenation capacity, *Biomechanics* 13 (2019), <https://doi.org/10.1063/1.5091492>, 034116.
- [12] J.A. Potkay, The promise of microfluidic artificial lungs, *Lab Chip* 14 (2014) 4122–4138, <https://doi.org/10.1039/c4lc00828f>.
- [13] A.A. Gimbel, E. Flores, A. Koo, G. García-Cardena, J.T. Borenstein, Development of a biomimetic microfluidic oxygen transfer device, *Lab Chip* 10 (2016) 1047, <https://doi.org/10.1039/C6LC00641H>.
- [14] E.R. Weibel, *The Pathway for Oxygen: Structure and Function in the Mammalian Respiratory System*, Harvard University Press, 1984 (1984)&ots=wPp6KsesXo&sig=BPn4ksEMV2ijzeabJycVNrfsfTE#v=onepage&q&f=false (accessed May 29, 2019), <https://books.google.ca/books?hl=en&lr=&id=OiDKzm9zmz8C&oi=fnd&pg=PA1&dq=E.+Weibel,+The+Pathway+for+Oxygen:+Structure+and+Function+in+the+Mammalian+Respiratory+System:+Harvard+University+Press.+272+300+p.+>
- [15] M.T. Newhouse, J. Strand, Tennis anyone? The lungs as a new court for systemic therapy, *CMAJ (Can. Med. Assoc. J.)* 161 (1999) 1287–1288.
- [16] K.M. Kovach, M.A. LaBarbera, M.C. Moyer, B.L. Cmolik, E. van Lunteren, A. Sen Gupta, J.R. Capadona, J.A. Potkay, In vitro evaluation and in vivo demonstration of a biomimetic, hemocompatible, microfluidic artificial lung, *Lab Chip* 15 (2015) 1366–1375, <https://doi.org/10.1039/c4lc01284d>.

- [17] A.J. Thompson, L.H. Marks, M.J. Goudie, A. Rojas-Pena, H. Handa, J.A. Potkay, A small-scale, rolled-membrane microfluidic artificial lung designed towards future large area manufacturing, *Biomicrofluidics* 11 (2017), <https://doi.org/10.1063/1.4979676>, 024113.
- [18] M. Dabaghi, N. Saraei, G. Fusch, N. Rochow, J.L. Brash, C. Fusch, P. R. Selvaganapathy, An ultra-thin highly flexible microfluidic device for blood oxygenation, *Lab Chip* 18 (2018) 3780–3789, <https://doi.org/10.1039/C8LC01083H>.
- [19] A.J. Thompson, L.J. Ma, T.J. Plegue, J.A. Potkay, Design analysis and optimization of a single-layer PDMS microfluidic artificial lung, *IEEE Trans. Biomed. Eng.* 66 (2019) 1082–1093, <https://doi.org/10.1109/TBME.2018.2866782>.
- [20] B.D. Kozower, B.F. Meyers, M.A. Smith, N.C. De Oliveira, S.D. Cassivi, T.J. Guthrie, H. Wang, B.J. Ryan, K.R. Shen, T.M. Daniel, D.R. Jones, The impact of the lung allocation score on short-term transplantation outcomes: a multicenter study, *J. Thorac. Cardiovasc. Surg.* 135 (2008) 166–171, <https://doi.org/10.1016/j.jtcvs.2007.08.044>.
- [21] M.C. Kung, J.-K. Lee, H.H. Kung, L.F. Mockros, Microchannel technologies for artificial lungs: (2) screen-filled wide rectangular channels, *Am. Soc. Artif. Intern. Organs J.* 54 (2008) 383–389, <https://doi.org/10.1097/MAT.0b013e31817ed9c8>.
- [22] J. a Potkay, M. Magnetta, A. Vinson, B. Cmolik, Bio-inspired, efficient, artificial lung employing air as the ventilating gas, *Lab Chip* 11 (2011) 2901–2909, <https://doi.org/10.1039/c1lc20020h>.
- [23] D.M. Hoganson, H.I. Pryor, E.K. Bassett, I.D. Spool, J.P. Vacanti, Lung assist device technology with physiologic blood flow developed on a tissue engineered scaffold platform, *Lab Chip* 11 (2011) 700–707, <https://doi.org/10.1039/c0lc00158a>.
- [24] T. Kniazeva, A.A. Epshteyn, J.C. Hsiao, E.S. Kim, V.B. Kolachalama, J.L. Charest, J. T. Borenstein, Performance and scaling effects in a multilayer microfluidic extracorporeal lung oxygenation device, *Lab Chip* 12 (2012) 1686–1695, <https://doi.org/10.1039/c2lc21156d>.
- [25] T. Rieper, C. Muller, H. Reinecke, Novel scalable and monolithically integrated extracorporeal gas exchange device, *Biomed. Microdevices* 17 (2015) 1–10, <https://doi.org/10.1007/s10544-015-9982-5>.
- [26] C.D. Murray, The physiological principle of minimum work applied to the angle of branching of arteries, *J. Gen. Physiol.* 9 (1926) 835–841, <https://doi.org/10.1085/jgp.9.6.835>.
- [27] C.D. Murray, The physiological principle of minimum work.I. The vascular system and the cost of blood volume, *Proc. Natl. Acad. Sci. U. S. A* 12 (1926) 207–214.
- [28] M.P. Wolf, G.B. Salieb-Beugelaar, P. Hunziker, PDMS with designer functionalities—properties, modifications strategies, and applications, *Prog. Polym. Sci.* 83 (2018) 97–134, <https://doi.org/10.1016/j.progpolymsci.2018.06.001>.
- [29] O. Siggaard-Andersen, P.D. Wimberley, N. Fogh-Andersen, I.H. Gøthgen, Measured and derived quantities with modern pH and blood gas equipment: calculation algorithms with 54 equations, *Scand. J. Clin. Lab. Investig.* 48 (1988) 7–15, <https://doi.org/10.1080/00365518809168181>.
- [30] A.V. Hill, The combinations of hemoglobin with oxygen and with carbon monoxide, *Biochem. J.* 7 (1913) 471–480.
- [31] J.A. Clark, W.J. Federspiel, P.A.A. Clark, G.R. Cokelet, Oxygen delivery from red cells, *Biophys. J.* 47 (1985) 171–181, [https://doi.org/10.1016/S0006-3495\(85\)83890-X](https://doi.org/10.1016/S0006-3495(85)83890-X).